arXiv:2111.00209v3 [cond-mat.str-el] 4 Mar 2022

Excitonic Correlations, Spin-State Ordering, and Magnetic-Field Effects in One-Dimensional Two-Orbital Hubbard Model for Spin-Crossover Region

Koya Kitagawa[1] and Hiroaki Matsueda[2]

[1]*Department of Physics, Graduate School of Science, Tohoku University*
[2]*Department of Applied Physics, Graduate School of Engineering, Tohoku University*

The electronic properties of excitonic insulators have been examined precisely in recent years. Pictures of exciton condensation may be applied to the spin-state transition observed in perovskite cobalt oxides. We examine the crystal-field and magnetic-field dependences of spatial spin structures on the basis of the density matrix renormalization group method using a low-energy effective model for the one-dimensional two-orbital Hubbard model. We find an excitonic insulating (EI) phase and a spin-state ordering (SSO) phase in the intermediate region between low-spin and high-spin phases. In the EI phase, spin-triplet excitons are spatially fluctuating due to quantum effects, and an incommensurate spin correlation realizes. In the SSO phase, 3-fold or incommensurate SSO structures realize depending on the crystal-field splitting. These structures are stabilized as a result of the competition of exchange interactions between spin states.

1. Introduction

The spin and orbital degrees of freedom provide a variety of physics in strongly correlated electron systems such as transition metal compounds.[1)] Fe or Co ions in such compounds change their spin states in response to temperature and pressure. For these ions, the competition between the crystal-field splitting and the Hund coupling causes the spin-state transition in the $3d$ orbital. $LaCoO_3$ is a typical perovskite cobalt oxide that shows a spin-state transition. The magnetic susceptibility and electrical conductivity of $LaCoO_3$ increase rapidly as temprature increases below 100 K.[2,3)]

These temperature dependences are explained by three competing $3d$ electron configurations of the Co^{3+} ion, which are a low-spin state with $s = 0$ for $(t_{2g})^6(e_g)^0$, an intermediate-spin state with $s = 1$ for $(t_{2g})^5(e_g)^1$, and a high-spin state with $s = 2$ for $(t_{2g})^4(e_g)^2$. The competition between these spin states also causes exotic phenomena such as giant magnetoresistance,[4)] magnetic clustering,[5,6)] and ferroelectricity.[7)]

Recently, the possibility of realizing excitonic insulators has been suggested in both experimental and theoretical studies.[8–14)] In excitonic insulators, a macroscopic number of electron-hole pairs are spontaneously generated by Coulomb interaction, and the pairs move coherently. This is called exciton condensation. In the vicinity of the spin-state transition, the fluctuation between competing spin states results in the excitonic insulating (EI) state. Therefore, considering the EI phase is important around the spin-state transition.

In the perovskite cobalt oxide $Pr_{0.5}Ca_{0.5}CoO_3$, a first-order metal-insulator phase transition around 90K has attracted attention in regards to the excitonic insulator.[9,15)] A first-order phase transition observed in high-magnetic-field experiments on $LaCoO_3$ has also been discussed in terms of its spin-state transition and exciton condensation.[16–19)] Besides the EI phase, a spin-state ordering (SSO) phase is another candidate for the magnetically induced phase in $LaCoO_3$. In the SSO phase, the spin state is crystallized and shows a superlattice structure. Some spatial patterns have been suggested in numerical analyses.[11,16)] The SSO phase has been observed in $LaCoO_3$ thin films on substrates $[(LaAlO_3)_{0.3}(SrAl_{0.5}Ta_{0.5}O_3)_{0.7}]$, where various superlattice structures of spin states have been observed.[20–22)] In such thin-film experiments, we can vary the spin state by controlling the crystal-field splitting, which is determined by the lattice constant of the substrate.

As described above, in the spin-state transition, the EI and SSO phases can be realized due to the spin and orbital degrees of freedom of $3d$ electrons. To understand the physics in the spin-state transition comprehensively, we need to develop a theory of multi-orbital strongly correlated electron systems that takes into account various types of spin structures and exciton condensation.

In this study, we examine the realization of the EI phase and various types of SSO on the basis of numerical analysis of the two-orbital Hubbard model (TOHM), which is the simplest strongly correlated model that describes spin-state transition. In previous theoretical studies, the realization of EI and SSO phases in the two-dimensional (2D) TOHM was confirmed under the framework of mean-field approximation and DMFT.[11,12,23)] However, in analyses using these methods, the order parameters or the spatial structures are assumed. In this study, the density matrix renormal-

ization group method (DMRG)[24,25] is performed on a low-energy effective model of the one-dimensional (1D) TOHM. With DMRG, we can perform an accurate analysis with a large system size without any assumptions on the various types of orderings or their spatial structures. Although the dimensionality is limited to 1D due to the limitation of the DMRG, an accurate picture of a 1D quantum system can be a probe to understand 2D or 3D ones. The main goal of this study is to make a ground-state phase diagram for the 1D TOHM in the vicinity of spin-state transition and to reveal the spatial structure in each phase.

In the analysis of the ground state of the low-energy effective model of TOHM, we find a EI phase and a SSO phase in the intermediate region between the low-spin (LS) phase and the high-spin (HS) phase. In the EI phase, an incommensurate spin correlation occurs, and its characteristic wavenumber changes continuously depending on the crystal field splitting. In the SSO phase, various types of SSO structures are found depending on the crystal-field splitting. As a particularly stable SSO structure, the 3-fold structure of LS/HS/HS is stabilized as a result of competing interactions between the nearest spin states. In the analyses of magnetic-field effects, we find the existence of a Haldane gap not only in the HS phase but also in the EI phase. In the magnetization process in the LS phase, a magnetized EI phase is found. In the magnetization process in the EI phase, we find that the magnetization process splits into two different processes.

This paper is organized as follows. In Sect. 2, we derive a low-energy effective model from the TOHM and describe the typical properties of the model. In Sect. 3, we show the results of DMRG analyses: a ground-state phase diagram in Subsect. 3.1, spatial structures of the EI and SSO phases in Subsect. 3.2, a phase diagram in a magnetic field in Subsect. 3.3, and the property of the entanglement entropy in each phase in Subsect. 3.4. In Sect. 4, we summarize the paper.

2. Model and Method

We start with TOHM, which is defined as

$$\begin{aligned}\mathcal{H}_{\rm TOHM} =& -\sum_{\langle ij\rangle\lambda\sigma} t_\lambda \left(c^\dagger_{i\lambda\sigma}c_{j\lambda\sigma} + \text{H.c.}\right) + \Delta\sum_{i\sigma} n_{ia\sigma} \\ &+ U\sum_{i\lambda} n_{i\lambda\uparrow}n_{i\lambda\downarrow} + U'\sum_{i\sigma} n_{ia\sigma}n_{ib\sigma} \\ &+ J\sum_{i\sigma\sigma'} c^\dagger_{ia\sigma}c^\dagger_{ib\sigma'}c_{ia\sigma'}c_{ib\sigma} \\ &+ I\sum_{i\lambda\neq\lambda'} c^\dagger_{i\lambda\uparrow}c^\dagger_{i\lambda\downarrow}c_{i\lambda'\downarrow}c_{i\lambda'\uparrow}. \end{aligned} \tag{1}$$

We define the annihilating operator of an electron at site i, orbital $\lambda(=a,b)$, and spin $\sigma(=\uparrow,\downarrow)$ as $c_{i\lambda\sigma}$. The electron number operator is defined as $n_{i\lambda\sigma} = c^\dagger_{i\lambda\sigma}c_{i\lambda\sigma}$. The first term in Eq. (1) describes the electron hopping between the same orbitals at the nearest sites $\langle ij\rangle$ with its amplitude t_λ. The second term describes the crystal-field splitting with its amplitude Δ. The remaining terms represent the onsite Coulomb interactions, where U is the intra-orbital Coulomb interaction, U' is the inter-orbital Coulomb interaction, J is the Hund coupling, and I is the pair hopping. We use the relational equations for the Coulomb interactions in an isolated ion: $U = U' + 2J$ and $I = J$. We focus on the case in which two electrons exist per site on average.

In the case of the spin-state transition, where $t_\lambda \ll U, U', J, \Delta$, the low-energy effective Hamiltonian of Eq. (1) is derived by Kanamori et al.[26] by treating the electron hopping terms as perturbations and truncating high-energy bases. The local bases of the effective Hamiltonian are

$$|L\rangle = \left(fc^\dagger_{b\uparrow}c^\dagger_{b\downarrow} - gc^\dagger_{a\uparrow}c^\dagger_{a\downarrow}\right)|0\rangle, \tag{2}$$

$$|H_{+1}\rangle = c^\dagger_{a\uparrow}c^\dagger_{b\uparrow}|0\rangle, \tag{3}$$

$$|H_0\rangle = \frac{1}{\sqrt{2}}\left(c^\dagger_{a\uparrow}c^\dagger_{b\downarrow} + c^\dagger_{a\downarrow}c^\dagger_{b\uparrow}\right)|0\rangle, \tag{4}$$

$$|H_{-1}\rangle = c^\dagger_{a\downarrow}c^\dagger_{b\downarrow}|0\rangle, \tag{5}$$

where $|0\rangle$ is a vacuum. The factors in Eq. (2) are given as $f = 1/\sqrt{1+(\Delta'-\Delta)^2/I^2}$ and $g = \sqrt{1-f^2}$, where $\Delta' = \sqrt{\Delta^2+I^2}$. $|L\rangle$ is the LS state, where the amplitude of the one-site spin is $s = 0$. In the case of $I = 0$, then $f = 1$ and $g = 0$, and $|L\rangle$ is the state in which two electrons occupy the low-energy orbital. If I becomes finite, then $|L\rangle$ contains the state in which two electrons occupy the high-energy orbital as hybridization. $|H_{s^z=0,\pm1}\rangle$ are HS states, where the amplitude of the one-site spin is $s = 1$. In this paper, the terms "LS state" and "HS state" refer to the one-site bases and not refer to global ones.

We truncate the following high-energy bases which has two electrons in a site,

$$|uL\rangle = \left(gc^\dagger_{b\uparrow}c^\dagger_{b\downarrow} + fc^\dagger_{a\uparrow}c^\dagger_{a\downarrow}\right)|0\rangle, \tag{6}$$

$$|iL\rangle = \frac{1}{\sqrt{2}}\left(c^\dagger_{a\uparrow}c^\dagger_{b\downarrow} - c^\dagger_{a\downarrow}c^\dagger_{b\uparrow}\right)|0\rangle, \tag{7}$$

where $|uL\rangle$ is the state in which two electrons mainly occupies the high energy orbital, and $|iL\rangle$ is the state in which one electron in the high-energy orbital and the other electron in the low-energy orbital form a singlet. This state is regarded as the singlet-exciton state while $|H_{0,\pm1}\rangle$ are regarded as the triplet-exciton states. If $J > 0$, triplet-exciton states become more stable than the singlet one. This behaviour has been presented in previous study.[27] In this study, we focus on the spin-state transition, where Δ and J are large. In this region, $|uL\rangle$ and $|iL\rangle$ are negligible.

The second order perturbation of t_a and t_b on the on-site basis $\{|L\rangle, |H_{+1}\rangle, |H_0\rangle, |H_{-1}\rangle\}$ gives the following effective Hamiltonian,

$$\begin{aligned}\mathcal{H}^{\rm eff} =& E_H \sum_i P_{Hi} \\ &+ E_L \sum_i P_{Li} \\ &+ \delta E_{LL} \sum_{\langle ij\rangle} P_{Li} P_{Lj} \\ &+ \delta E_{HL} \sum_{\langle ij\rangle} (P_{Hi} P_{Lj} + P_{Li} P_{Hj}) \\ &+ J_s \sum_{\langle ij\rangle} (\vec{s}_i \cdot \vec{s}_j - 1) P_{Hi} P_{Hj} \\ &+ J' \sum_{\langle ij\rangle} \left[P_i^- (\vec{s}_i \cdot \vec{s}_j + 1) P_j^+ + \text{H.c.} \right] \\ &+ I' \sum_{\langle ij\rangle} \left[(\vec{s}_i \cdot \vec{s}_j - 1) P_i^+ P_j^+ + \text{H.c.} \right]. \end{aligned} \tag{8}$$

The operators in Eq. (8) are given as

$$P_{Li} = |L\rangle_i \langle L|_i , \tag{9}$$

$$P_{Hi} = \sum_{s^z=-1,0,1} |H_{s^z}\rangle_i \langle H_{s^z}|_i , \tag{10}$$

$$P_i^+ = |H_0\rangle_i \langle L|_i , \tag{11}$$

$$P_i^- = |L\rangle_i \langle H_0|_i . \tag{12}$$

The factors in Eq. (8) are given as

$$E_H = \Delta + U' - J, \tag{13}$$

$$E_L = \Delta + U - \Delta', \tag{14}$$

$$\delta E_{LL} = \frac{4f^2 g^2 (t_a^2 + t_b^2)}{2U' - U - J + 2\Delta'}, \tag{15}$$

$$\delta E_{HL} = (t_a^2 + t_b^2) \left[\frac{f^2}{-\Delta + U' + \Delta'} + \frac{g^2}{\Delta + U' + \Delta'} \right], \tag{16}$$

$$J_s = \frac{t_a^2 + t_b^2}{U + J}, \tag{17}$$

$$J' = 2t_a t_b \left[\frac{f^2}{-\Delta + U' + \Delta'} + \frac{g^2}{\Delta + U' + \Delta'} \right], \tag{18}$$

$$I' = 2t_a t_b fg \left[\frac{1}{U + J} + \frac{1}{2U' - U - J + 2\Delta'} \right]. \tag{19}$$

We introduce a spin and pseudospin representation[10] of Eq. (8) to clarify the anisotropy of the Hamiltonian. First, we introduce descending and ascending operators between the $s = 0$ LS state and $s = 1$ HS quadrupoles, which are defined as

$$P_X^- = \frac{1}{\sqrt{2}} (|L\rangle \langle H_{-1}| - |L\rangle \langle H_{+1}|), \tag{20}$$

$$P_Y^- = \frac{1}{\sqrt{2}i} (|L\rangle \langle H_{-1}| + |L\rangle \langle H_{+1}|), \tag{21}$$

$$P_Z^- = |L\rangle \langle H_0| , \tag{22}$$

$$P_\Gamma^+ = (P_\Gamma^-)^\dagger \quad (\Gamma = X, Y, Z). \tag{23}$$

Second, the pseudospin operators τ_Γ^γ for $\Gamma = X, Y, Z$ are defined with the descending and ascending operators in Eqs. (20)-(23) as

$$\tau_\Gamma^x = P_\Gamma^- + P_\Gamma^+, \tag{24}$$

$$\tau_\Gamma^y = i(P_\Gamma^- - P_\Gamma^+), \tag{25}$$

$$\tau_\Gamma^z = P_\Gamma^+ P_\Gamma^- - P_L. \tag{26}$$

Note that the representations of the pseudospin operators τ_Γ^γ are twice as much as the ones of the spin 1/2 operator. Finally, the spin and pseudospin representation of the effective Hamiltonian in Eq. (8) is

$$\begin{aligned}\mathcal{H}^{\rm eff} =& E_{0\tau} - h_{\tau z} \sum_i \tau_i^z + J_s \sum_{\langle ij\rangle} \vec{s}_i \cdot \vec{s}_j + J_z \sum_{\langle ij\rangle} \tau_i^z \tau_j^z \\ &+ J_x \sum_{\Gamma=X,Y,Z} \sum_{\langle ij\rangle} \tau_{\Gamma i}^x \tau_{\Gamma j}^x + J_y \sum_{\Gamma=X,Y,Z} \sum_{\langle ij\rangle} \tau_{\Gamma i}^x \tau_{\Gamma j}^x, \end{aligned} \tag{27}$$

where $\vec{s}$ is the spin operator whose amplitude is $s = 1$, and $\tau_i^z = \tau_{Xi}^z + \tau_{Yi}^z + \tau_{Zi}^z$. Note that the spin operator $\vec{s}$ is generally not commutative with the pseudospin operator τ_Γ^γ. The factors in Eq. (27) are given as

$$E_{0\tau} = NE_L - \frac{Nn_z \delta E_{LL}}{2} + \frac{3N\tilde{\Delta}}{4} + \frac{9Nn_z J_n}{32}, \tag{28}$$

$$-h_{\tau z} = -\left(\frac{\tilde{\Delta}}{4} + \frac{3n_z J_n}{16} \right), \tag{29}$$

$$J_x = \frac{J' + I'}{2}, \tag{30}$$

$$J_y = \frac{J' - I'}{2}, \tag{31}$$

$$J_z = \frac{J_n}{16}, \tag{32}$$

where

$$\tilde{\Delta} = E_H - E_L + n_z(\delta E_{LL} - \delta E_{HL}), \tag{33}$$

$$J_n = 2\delta E_{HL} - \delta E_{LL} - J_s, \tag{34}$$

where n_z is number of the nearest sites, and $z = 2$ in the 1D system. When I is nonzero in Eq. (1), then $J_x > J_y$ in Eq. (27), and the number of excitons (HS states) does not conserve. Naively, the anisotropy of $J_x > J_y$ in the pseudospin-pseudospin interaction seems to induce a long-range order for $\langle \tau_{\Gamma i}^x \rangle$. However, since there are spin-

spin and the other pseudospin-pseudospin interactions in Eq. (27), the long-range order for $\langle \tau^x_{\Gamma i} \rangle$ can be suppressed as a result of the competition of the interactions. In fact, no symmetry breakings of $\langle \tau^x_{\Gamma i} \rangle$ are obtained in this study. In addition to Eq. (27), the Zeeman energy term is introduced as

$$\mathcal{H}_{\rm Zeeman} = -H \sum_i s^z_i. \tag{35}$$

Before showing the results of the numerical analysis in Sect. 3, we show in Table I the typical configurations of pseudospins in the effective model in Eq. (27), where spin degrees of freedom and quantum fluctuations are not taken into consideration.

Table I. Typical configurations of pseudospins in effective model in Eq. (27).

Phase	τ_Γ configurations	Parameter conditions
LS	$\downarrow\ \downarrow\ \downarrow\ \downarrow$	$h_{\tau z} \ll 0\ (\Leftrightarrow \Delta \gg U - U' + J)$
HS	$\uparrow\ \uparrow\ \uparrow\ \uparrow$	$h_{\tau z} \gg 0\ (\Leftrightarrow \Delta \ll U - U' + J)$
EI	$\rightarrow\ \leftarrow\ \rightarrow\ \leftarrow$	$h_{\tau z} \sim 0,\ J_x > J_y > J_z$
		$(\Leftrightarrow \Delta \sim U - U' + J,\ t_a/t_b \sim 1)$
SSO	$\uparrow\ \downarrow\ \uparrow\ \downarrow$	$h_{\tau z} \sim 0,\ J_x, J_y \ll J_z$
		$(\Leftrightarrow \Delta \sim U - U' + J,\ t_a/t_b \sim 0)$

In the case of $\Delta \gg U - U' + J$, where the crystal-field splitting is sufficiently large, $h_{\tau z} \ll 0$ in the effective model in Eq. (27), and the ground state is in a low-spin (LS) phase with $(\tau_\Gamma : \downarrow \downarrow \ \ldots \ \downarrow)$. In the case of $\Delta \ll U - U' + J$ and $h_{\tau z} \gg 0$, the ground state is in a high-spin (HS) phase with $(\tau_\Gamma : \uparrow \uparrow \ \ldots \ \uparrow)$. In the case where Δ and $U - U' + J$ are comparable, the inter-pseudospin interaction J_γ and the inter-spin interaction J_s are dominant. The inter-pseudospin interaction J_γ is anisotropic for $\gamma = x, y, z$. Since $J_z \propto t_a^2 + t_b^2$ and $J_x, J_y \propto 2t_a t_b$, the behavior of the ground state depends on the parameter $\eta = 2t_a t_b/(t_a^2 + t_b^2)$, which characterizes the anisotropy of the pseudospin-pseudospin interaction. The range of η is $0 \le \eta \le 1$, where $t_a/t_b = 0$ for $\eta = 0$, and $t_a/t_b = 1$ for $\eta = 1$. In the case of $\eta \ll 1$, the anisotropy becomes $J_z \gg J_x, J_y$, and the ground state tends to show a SSO with $(\tau_\Gamma : \uparrow \downarrow \ \ldots \ \uparrow \downarrow)$. If η is not small, the anisotropy can be $J_z < J_y < J_x$, and pseudospins tend to form a state in which the pseudospin points in the x axis, $(\tau_\Gamma : \rightarrow \leftarrow \ \ldots \ \rightarrow \leftarrow)$. In this configuration, the LS and HS states are hybridized. Since the HS state is regarded as a spin-triplet exciton, the configuration $(\tau_\Gamma : \rightarrow \leftarrow \ \ldots \ \rightarrow \leftarrow)$ represents the EI configuration, in which the excitons move coherently. In practice, the picture of the ground state of the effective model becomes more complicated due to the competition of multiple interactions in Eq. (27), which include the spin-spin interaction and three types of pseudospin-pseudospin interactions identified by $\Gamma = X, Y, Z$.

We apply the DMRG method to the effective model. The system is 1D and has the open boundary condition unless otherwise specified. We set the truncation number in DMRG to $\chi = 256$ (and exceptionally $\chi = 64$ to determine some phase boundaries). Under this setting, the truncation error of the reduced density matrix is less than 10^{-5}. We additionally use the periodic boundary condition for analyses of the SSO phase, where incommensurate spin structures are found.

3. Results

3.1 Ground-state phase diagram

In this subsection, we present phase diagrams obtained by the numerical analysis with DMRG.

First, we fix the anisotropy factor for the pseudospin interaction at $\eta = 1\ (\Leftrightarrow t_a = t_b)$ and make a phase diagram in the plane of the Hund coupling J and the crystal-field splitting Δ, where we set the parameters of the Coulomb interactions to $U/\sqrt{t_a^2 + t_b^2} = 12$, $U' = U - 2J$, and $J = I$ as a strongly correlated region. The Δ-J phase diagram is shown in Fig. 1(a). In Fig. 1(a), as Δ increases, the phase shifts as HS $\rightarrow$ EI $\rightarrow$ LS, where HS, EI, and LS stand for a low-spin phase, an excitonic insulating phase, and a high-spin phase, respectively. The phase transitions at HS-EI and EI-LS are second-order transitions. We obtain the phase boundaries by the discontinuity of the entanglement entropy, which is discussed in Subsect. 3.4.

In Fig. 1(b), we present the populations of the HS state $\langle P_H \rangle$ and LS state $\langle P_L \rangle$ along the dashed line in Fig. 1(a). In the EI phase, the LS state and the HS state coexist, and the population of the LS state increases as Δ increases.

We can understand the property of the EI phase in the nearest correlation functions. We show the nearest correlation functions, $\langle \tau^x_{\Gamma i} \tau^x_{\Gamma i+1} \rangle$, $\langle \tau^y_{\Gamma,i} \tau^y_{\Gamma,i+1} \rangle$, $\langle \tau^z_{\Gamma,i} \tau^z_{\Gamma,i+1} \rangle$, and $\langle s^z_i s^z_{i+1} \rangle$ in Fig. 1(c). Note that the product of the nearest pseudospin, $\langle \tau^z_{\Gamma i} \rangle \langle \tau^z_{\Gamma i+1} \rangle$, is not subtracted from $\langle \tau^z_{\Gamma i} \tau^z_{\Gamma i+1} \rangle$ although $\langle \tau^z_{\Gamma j} \rangle$ is positive in the HS phase and negative in the LS phase. We compute the correlation function at the center of the system. The values of the pseudospin correlations are independent of the quadrupole basis $\Gamma = X, Y, Z$ because of the rotational symmetry. The large value of $|\langle \tau^x_{\Gamma,i} \tau^x_{\Gamma,i+1} \rangle|$ in the EI phase indicates that the EI phase is stabilized by the local kinetic energy of excitons. Compared with $\langle \tau^x_{\Gamma,i} \tau^x_{\Gamma,i+1} \rangle$, $\langle \tau^y_{\Gamma,i} \tau^y_{\Gamma,i+1} \rangle$ does not show strong antiferromagnetism. This is because the antiferromagnetic interactions between pseudospins satisfy $J_x > J_y$. $\langle \tau^z_{\Gamma,i} \tau^z_{\Gamma,i+1} \rangle$ also does not show strong antiferromagnetism even near the center of the EI phase as a result of $J_x > J_z$. Near the HS(LS) phase, large value of $-h_{\tau z}$ ($h_{\tau z}$) makes $\langle \tau^z_{\Gamma,i} \tau^z_{\Gamma,i+1} \rangle$ ferromagnetic. In terms of long-range correlation functions, $\langle \tau^x_{\Gamma i} \tau^x_{\Gamma j} \rangle$ and $\langle \tau^y_{\Gamma i} \tau^y_{\Gamma j} \rangle$ become zero at $|i - j| \to \infty$. This means that there is no long-range order in the EI phase, that is $\langle \tau^x_{\Gamma i} \rangle = \langle \tau^y_{\Gamma i} \rangle = 0$ for $\Gamma = X, Y, Z$

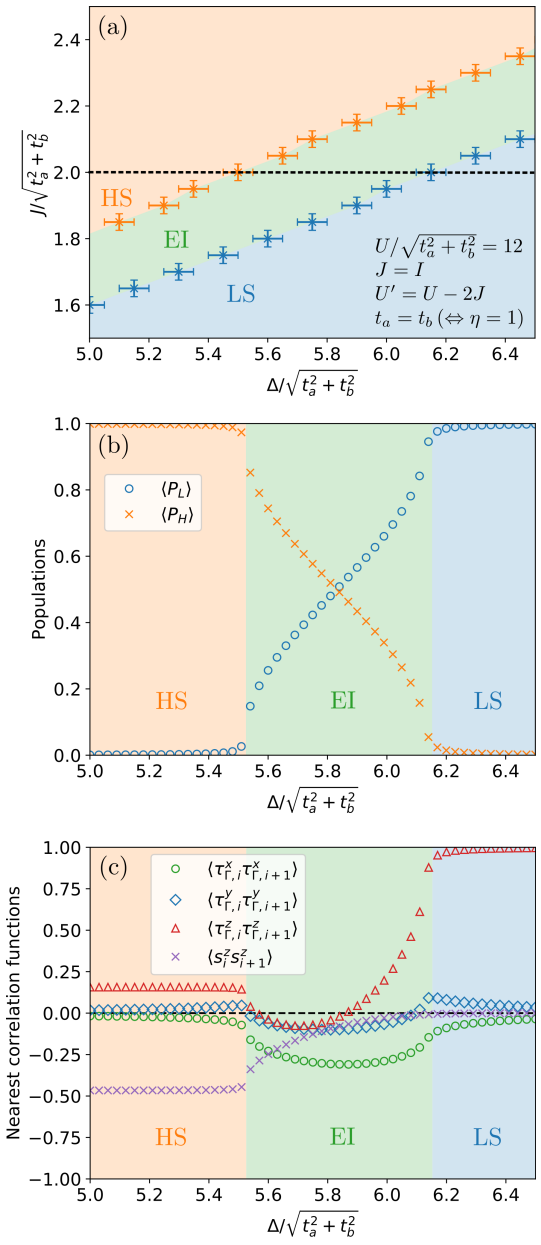

Fig. 1. Panel (a) shows a ground-state phase diagram for the effective Hamiltonian in Eq. (27) in the plane of the Hund coupling $J/\sqrt{t_a^2+t_b^2}$ and the crystal-field splitting $\Delta/\sqrt{t_a^2+t_b^2}$, where we set the parameters as $U/\sqrt{t_a^2+t_b^2}=12$ and $\eta=1\,(\Leftrightarrow t_a=t_b)$. Panel (b) shows the populations of the LS and HS states along the dashed line in panel (a), where $J/\sqrt{t_a^2+t_b^2}=2$. Panel (c) shows the nearest correlation functions along the dashed line in Panel (a).

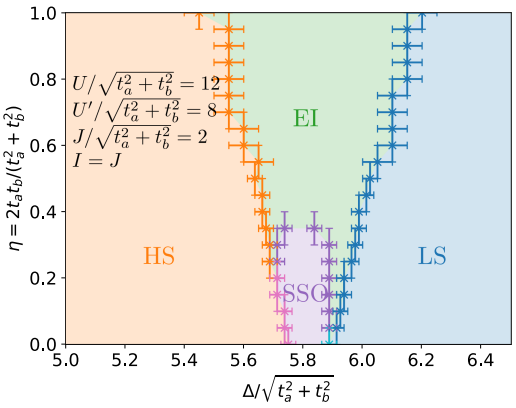

Fig. 2. A ground-state phase diagram for the effective Hamiltonian in Eq. (27) in the plane of the anisotropy factor for pseudospin η and the crystal-field splitting $\Delta/\sqrt{t_a^2+t_b^2}$, where we fix that $U/\sqrt{t_a^2+t_b^2}=12$ and $J/\sqrt{t_a^2+t_b^2}=2$. The error bars represent discrete intervals for the analysis.

and i at any site. Since there are spin-spin interaction and three types of pseudospin-pseudospin interactions identified by Γ in Eq. (27), the long-range order of EI can be suppressed as a result of the competition of the interactions.

The nearest spin correlation $\langle s_i^z s_{i+1}^z\rangle$ in Fig. 1(c) is antiferromagnetic in the HS and EI phases. In the HS phase, $\langle P_H\rangle\sim 1$. In this region, the effective Hamiltonian reduces to the antiferromagnetic $s=1$ Heisenberg model, and the nearest spin correlations becomes negative. In the EI phase, $\langle P_H\rangle$ is finite, and antiferromagnetic spin-spin interaction between the HS states make the nearest spin correlation negative.

Next, we present a phase diagram in the plane of the anisotropy for the pseudospin interaction η and the crystal-field splitting Δ in Fig. 2, where we fix the parameters of Coulomb interactions to $U/\sqrt{t_a^2+t_b^2}=12$, $U'/\sqrt{t_a^2+t_b^2}=8$, and $J/\sqrt{t_a^2+t_b^2}=I/\sqrt{t_a^2+t_b^2}=2$. In addition to the HS, EI, and LS phases, the SSO phase is found in Fig. 2. In the SSO phase, the spin states show superlattice structures, in which the population of HS states varies from site to site. The spatial structure of SSO changes depending on Δ and η. We focus on the spatial structures in the next subsection.

We characterize the SSO phase on the basis of the existence of a superstructure of spin states. The criterion is that a state is in the SSO phase when $\max(\langle P_{Hi}\rangle)-\min(\langle P_{Hi}\rangle)>10^{-2}$ for i in the central 20 sites in a 60-sites system with open boundaries.

The outlines in the phase diagrams in Fig. 1 and Fig. 2 can be understood as the typical configurations of pseudospins which is shown in Table I, and is consistent with the previous studies.[10,19] However, no spin or pseudospin ordering is observed in the HS and EI phases. This is interpreted as the result of the effect of strong quantum fluctuations in a 1D system, which is considered in the DMRG method. In addition, various types of spin-state structures were obtained by using large 1D clusters.

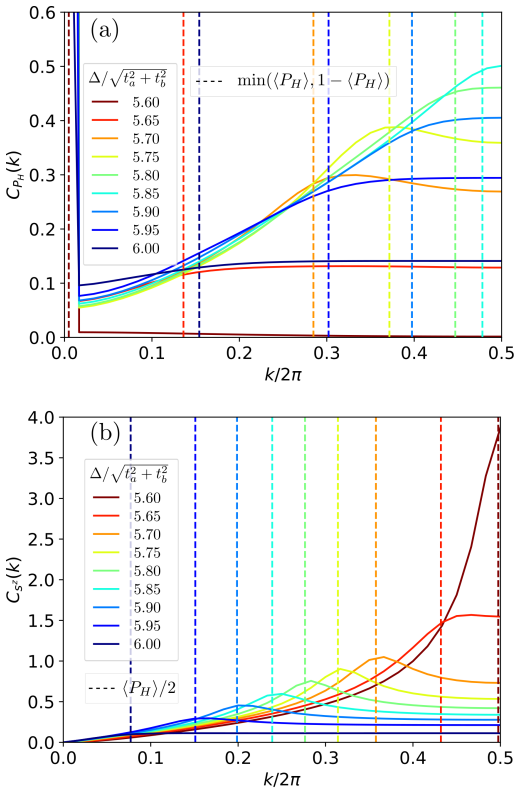

Fig. 3. Fourier transformed correlation functions in the EI phase. Panel (a) shows the correlations of HS state $C_{P_H}(k)$ at $\eta = 0.5$ for some $\Delta/\sqrt{t_a^2+t_b^2}$. The dashed lines in panel (a) are the expected values of $\min(\langle P_H\rangle, 1-\langle P_H\rangle)$ per site. Panel (b) shows the spin correlation $C_{s^z}(k)$ at $\eta = 0.5$. The dashed lines in panel (b) are $\langle P_H\rangle/2$.

3.2 Spatial structures of spin states in the EI and SSO phases

In this subsection, we present the spatial structures of the spin states in the EI phase and the SSO phase through correlation functions. We set the system size as $L = 60$ and use the periodic boundary condition.

We consider a Fourier transformed correlation functions for spin states as

$$C_X(k) = \frac{1}{L}\sum_{ij}\langle X_i X_j\rangle \cos\left[k(i-j)\right], \qquad (36)$$

where X_i is a one-site operator at a site i. Note that the product of one-site expected values are not subtracted in $C_X(k)$.

First, we fix the parameters as $U/\sqrt{t_a^2+t_b^2} = 12, J/\sqrt{t_a^2+t_b^2} = I/\sqrt{t_a^2+t_b^2} = 2, U' = U-2J, \eta = 0.5$. In this region, the phase transition is HS $\to$ EI $\to$ LS as $\Delta/\sqrt{t_a^2+t_b^2}$ increases.

In Fig. 3(a), we present the correlation function for the HS state $C_{P_H}(k)$ in the EI phase. Since $\langle P_{Hi}\rangle$ is uniform in the EI phase, k-dependence of $C_{P_H}(k>0)$ corresponds to the spatial quantum fluctuation in the

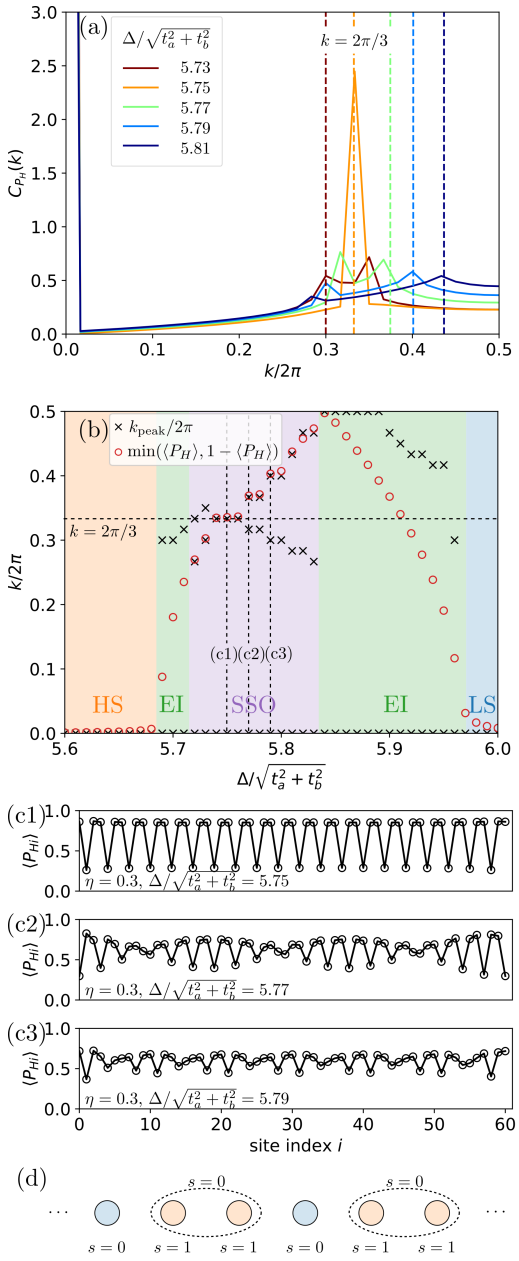

Fig. 4. Fourier transformed correlation functions in the SSO phase. Panel (a) shows the correlations of HS state $C_{P_H}(k)$ at $\eta = 0.3$ for some $\Delta/\sqrt{t_a^2+t_b^2}$. The dashed lines are the expected values of $\min(\langle P_H\rangle, 1-\langle P_H\rangle)$. Panel (b) shows the peak wavenumber against the crystal-field splitting $\Delta/\sqrt{t_a^2+t_b^2}$. In Panels (c1), (c2), and (c3), some SSO structures obtained in the SSO phase are shown. Each parameter corresponds to the dashed line in panel (b). Panel (d) shows the schematic picture of the LS/HS/HS structure in Panel (c1).

population of HS states. $C_{P_H}(k=0)$ originates in the uniform populations of the HS state. k-dependence of $C_{P_H}(k>0)$ is small in the HS phase and the LS phase and becomes large in the EI phase. This behavior means that, in the EI phase, there is a strong quantum fluctua-

tion, and the ground state is far from the direct product state such as $(\tau_\Gamma :\rightarrow \leftarrow \cdots \rightarrow \leftarrow)$, in which $C_{P_H}(k>0)$ is constant. In Fig. 3(a), we also show the wave number at $2\tilde{k} = \min(2\pi \langle P_H \rangle, 2\pi(1-\langle P_H \rangle))$ by broken lines, where $\langle P_H \rangle$ is the spatial average of the populations of HS states. If excitons are regarded as free fermions, $\tilde{k}$ is interpreted as the Fermi wavenumber. In the EI phase, $C_{P_H}(k>0)$ tends to rise as k increases in $k<\tilde{k}$ and becomes constant in $k>\tilde{k}$. This behavior is similar to the behavior of 1D spinless free fermions. As a difference from the case of fermions, $C_{P_H}(k\to 0)$ is non-zero in the EI phase. This originates in the anisotropy of $J_x > J_y$ in Eq. (27), which means the number of excitons does not conserve.

In Fig. 3(b), we show the Fourier transformed spin correlation $C_{s^z}(k)$ with the same parameters as those in Fig. 3(a). $C_{s^z}(k)$ has a peak at $k=\pi\langle P_H\rangle$ in the EI and HS phases. This is interpreted as the spin correlation in the EI phase representing a spin density wave whose wavenumber corresponds to the population of the HS state, although there is no spin ordering.

Next, we fix $\eta = 0.3$. In this region, the phase transitions are HS $\to$ EI $\to$ SSO $\to$ EI $\to$ LS as $\Delta/\sqrt{t_a^2+t_b^2}$ increases. Figure 4(a) shows $C_{P_H}(k)$ in the SSO phase. We also show the peak wavenumbers against the crystal-field splitting in Fig. 4(b). The sharp peaks in Fig. 4(a) represent the structure of the SSO. There is a strong peak for $k=2\pi/3$ in $\Delta/\sqrt{t_a^2+t_b^2}=5.75$. This peak represents the LS/HS/HS structure shown in Fig. 4(d).

As shown in Fig. 4(b), the spin-state structure in the SSO phase changes against the crystal-field splitting $\Delta/\sqrt{t_a^2+t_b^2}$. The plateau at $k=2\pi/3$ in Fig. 4(b) indicates that the LS/HS/HS structure is stable. According to the Hamiltonian in Eq. (27), the nearest LS-HS pair is stabilized by the J_z term, and the nearest HS-HS pair is stabilized by the J_s term. The LS/HS/HS structure is realized as a result of the competition between these interactions. In the other region in the SSO phase, two peaks branch from the peak at $k=2\pi/3$. The two peaks have generally incommensurate wavenumbers, and one of them follows the population of the HS state $\langle P_H\rangle$. The discretization of the $k_{\rm peak}$ in Fig. 4(b) seems to originate from the finite system size $L=60$ and should become continuous in $L\to\infty$. Some snapshots of the spin-state structures in the SSO phase are shown in Fig. 4(c1)-(c3). Figure 4(c1) shows the LS/HS/HS structure shown in Fig. 4(d). Figure 4(c2) shows the structure at $\Delta/\sqrt{t_a^2+t_b^2}=5.77$, which is near the parameter at which LS/HS/HS structure realizes. Here some kinks are inserted into the basic LS/HS/HS structure. Figure 4(c3) shows the structure at $\Delta/\sqrt{t_a^2+t_b^2}=5.79$, which is far from the parameter of LS/HS/HS structure. Here a complex spin state is found. In the region where $\langle P_H\rangle < 0.5$, the SSO phase is not found. This result indicates that the spin-spin interaction between the HS states contributes to the stabilization of the SSO with the LS/HS/HS structure.

3.3 Magnetic-field effects

In this subsection, we present the magnetic-field effects in the effective model. Figures 5(a) and 5(b) are phase diagrams in the plane of the crystal-field splitting $\Delta/\sqrt{t_a^2+t_b^2}$ and a magnetic field $H/\sqrt{t_a^2+t_b^2}$, where we fix the parameters, $U/\sqrt{t_a^2+t_b^2}=12$, $J/\sqrt{t_a^2+t_b^2}=I/\sqrt{t_a^2+t_b^2}=2$, $U'=U-2J$ and $\eta=1$ ($\Leftrightarrow t_a=t_b$). In these parameters, the EI phase exists in the intermediate region between the HS and LS phases. In Figs.5(a) and 5(b), in addition to the HS, EI, and LS phases, there appears a type-1 magnetized excitonic insulating phase (MEI-1), a type-2 magnetized excitonic insulating phase (MEI-2), a magnetized high-spin phase (MHS), and a fully polarized phase (Full Polar). All the phase transitions are second-order ones. We determine the phase boundary on the basis of the discontinuity of the first derivative of the magnetization curve. Basically, we set the system size as $L=60$ and set the truncation number in DMRG as $\chi=64$.

The value of a magnetic field at the phase boundaries for HS-MHS, EI-MEI-2, and LS-MEI-1 corresponds to the spin gaps in HS, EI, and LS phases, respectively. As shown in Figs.5(a) and 5(b), spin gaps are obtained in the HS, EI, and LS phases, and the spin gaps seem to close at the EI-LS phase boudnary. To determine the spin gaps in the HS and EI phases, system-size extrapolations are performed. The extrapolation is performed with the function

$$\Delta_s(L) = \Delta_s(\infty) + a/L + b/L^2, \tag{37}$$

where $\Delta_s(\infty)$, a, and b are the fitting parameters. $\Delta_s(L)$ is a spin gap in the system whose size is L. $\Delta_s(L)$ is computed by $\Delta_s(L) = E^{(m=2)}(L) - E^{(m=0)}(L)$, where $E^{(m)}(L)$ is the energy of the ground state at $\langle \sum_i s_i^z \rangle = m$. We avoid $E^{(m=1)}(L) - E^{(m=0)}(L)$ because it corresponds to the spin excitation at the edges in AKLT model, and this magnetization can be ignored in an infinite system. We use $L=128, 192, 256$ under the open boundary condition and set the truncation number in DMRG to $\chi=256$. Some examples for the L dependence of the $\Delta_s(L)$ are shown in Fig. 6. Figure 6(a) and (b) show that there is a finite spin gap in the HS and EI phases. In the EI phase near the LS phase of $5.80 < \Delta/\sqrt{t_a^2+t_b^2} < 6.15$, the spin gap becomes small and its existence is not obtained with sufficient accuracy. Therefore, we omit the points in this region.

The spin gap in the HS phase is the Haldane-gap because in $\Delta \ll U-U'+J$, the low-energy effective Hamiltonian in Eq. (27) reduces to the $s=1$ Heisenberg model. In fact, the value of the spin gap in the HS phase in Fig. 5(b) is in good agreement with $\Delta_s = \Delta_{\rm Haldane} J_s = 0.0293$, where $J_s = (t_a^2+t_b^2)/(U+J) = 0.0714\ldots$ is the amplitude of spin-spin interaction in Eq. (27), and

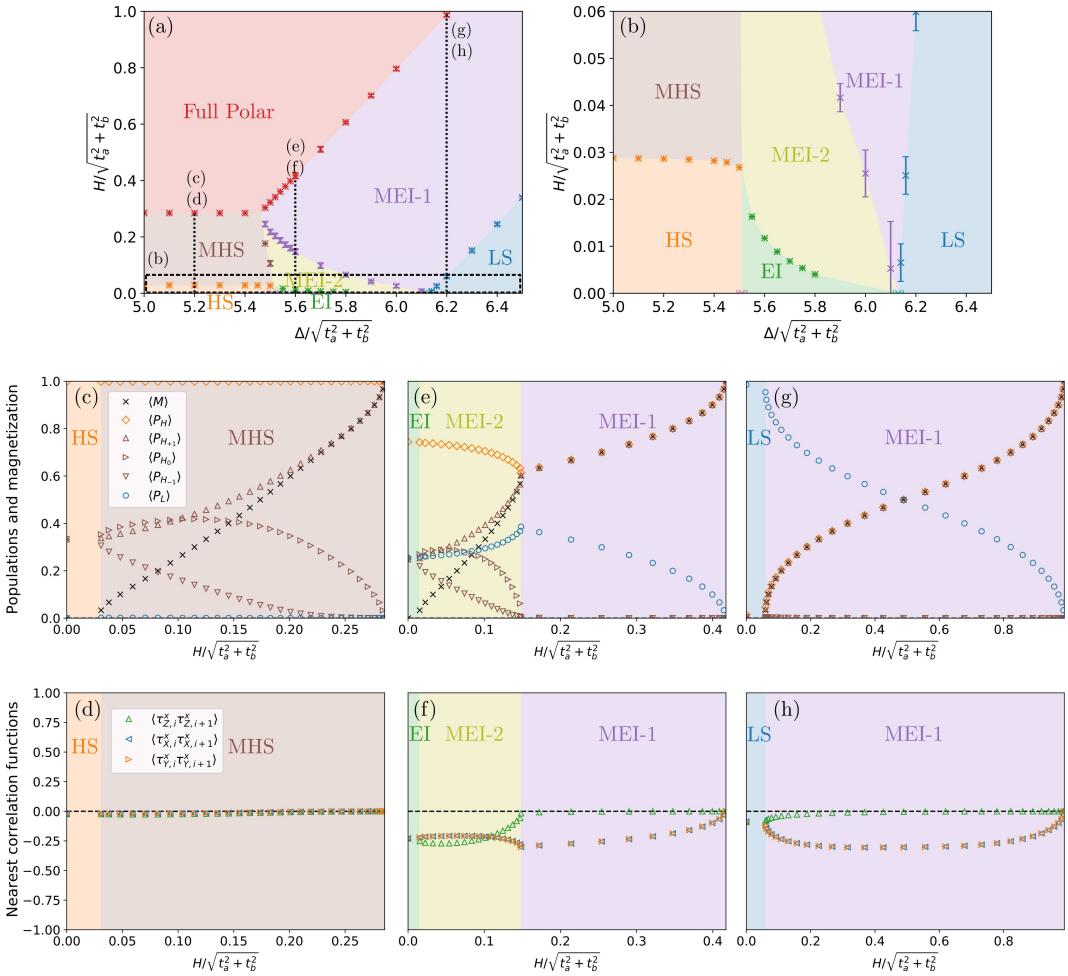

Fig. 5. Phase diagram of the effective model in a magnetic field. Panel (a) is phase diagram in the plane of a magnetic field $H/\sqrt{t_a^2+t_b^2}$ and crystal-field splitting $\Delta/\sqrt{t_a^2+t_b^2}$. Panel (b) is the enlarged view of the low magnetic-field region enclosed by the dashed line in panel (a). The error bars in Panels (a) and (b) represent the discretization of the magnetization in the finite system size $L = 60$. Exceptionally, the phase boundaries at the HS-MHS and the EI-MEI-2 are determined by the extrapolation. The dashed lines in panel (a) represent the magnetization processes in panels (c)-(h). Panels (c), (e), and (g) shows the magnetization curve and the populations of spin states in the magnetization process in the HS, EI, and LS phases, respectively. Panels (d), (f), and (h) show nearest pseudospin correlations in the magnetization process in the HS, EI, and LS phases, respectively.

$\Delta_{\rm Haldane} = 0.4105$ is the value of Haldane gap of $s = 1$ Heisenberg model obtained in the previous study.[25)]

The spin gap in the EI phase is similar to the one of $s = 1$ Heisenberg model as follows. First, the value of spin gap in the EI phase connects to the one in the HS phase. Second, the ground state energies in the EI phase degenerate for $m = 0, \pm 1$ under the open boundary condition, and the degeneracy lifts under the periodic boundary condition. Therefore, it is suggested that the degeneracy has its origin in the free 1/2-spins at edges.

The spin gap in the LS phase is due to the energy difference between the LS state and the HS state.

From here, we present the magnetization processes in the phases along the dashed lines (c)-(h) in Fig. 5(a).

The magnetization process in a wide range of the HS phase is HS $\rightarrow$ MHS $\rightarrow$ Full Polar (the dashed line at (c) and (d) in Fig. 5(a)). In the MHS phase, the population of the LS state is almost zero, and $\langle\tau^x_{\Gamma,i}\tau^x_{\Gamma,i+1}\rangle$ is almost zero. Therefore, the magnetization process in the MHS phase is the process in which $s = 1$ spins are aligned by a magnetic field.

The magnetization process in the EI phase is EI $\rightarrow$ MEI-2 $\rightarrow$ MEI-1 $\rightarrow$ Full Polar (the dashed line at (e) and (f) in Fig. 5(a)), where we call the MEI phase in a low magnetic field MEI-2 and the phase in a high magnetic field MEI-1. As shown in Fig. 5(e), in the MEI-2 phase, the population of the HS state is finite for all bases of $s^z = +1, 0, -1$, whereas in the MEI-1 phase, the populations of $s^z = +1$ is finite, and that of $s^z = 0, -1$ is almost zero. Therefore, the phase transition of MEI-2 $\rightarrow$ MEI-1

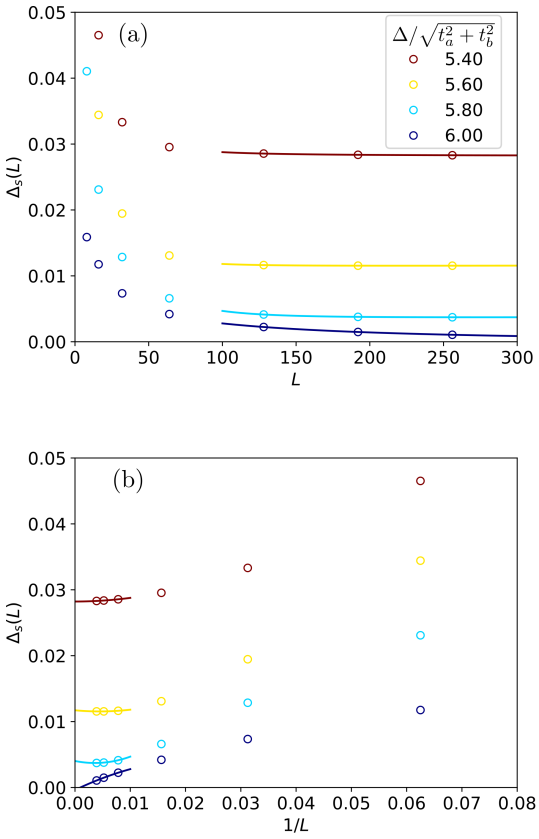

Fig. 6. Spin gap extrapolations with Eq. (37). Panel (a) shows L dependence of $\Delta_s(L)$, and panel (b) shows $1/L$ dependence of $\Delta_s(L)$. $\Delta/\sqrt{t_a^2+t_b^2}=5.40$ is in the HS phase, and the others are in the EI phase. $\Delta/\sqrt{t_a^2+t_b^2}=6.00$ is near the LS phase and we cannot find the finite spin gap. We discard this in Fig. 5.

occurs when the $s=1$ spins are fixed to $s^z=+1$ by a magnetic field. Because of the antiferromagnetic spin-spin interaction, MEI-2 phase survives even in a finite magnetic field. Regarding the nearest correlation functions shown in Fig. 5(f), while $\langle\tau^x_{\Gamma,i}\tau^x_{\Gamma,i+1}\rangle$ for $\Gamma=X,Y,Z$ are all negative in the MEI-2 phase, $\langle\tau^x_{Z,i}\tau^x_{Z,i+1}\rangle$ is almost zero in the MEI-1 phase. This means that the MEI-1 phase is stabilized by the kinetic energy of $s^z=+1$ excitons. Since $|H_{s^z=+1}\rangle=-(P^+_X|L\rangle+iP^+_Y|L\rangle)/\sqrt{2}$, the X and Y excitons coexist with the z-direction magnetization, while the Z excitons compete with the magnetization. As a result, in the MEI-2 phase, the X, Y, and Z excitons are stabilized, while in the MEI-1 phase, only $s^z=+1$ exciton is stabilized.

The magnetization process in the LS phase is LS $\rightarrow$ MEI-1 $\rightarrow$ Full Polar (the dashed line at (g) and (h) in Fig. 5(a)). The MEI-1 phase is the same phase as in the magnetization process in the EI phase. As shown in Figs. 5(g) and 5(h), the properties of the populations and the nearest correlations are consistent with the MEI-1 phase in the magnetization process in the EI phase.

In Fig. 5(a), we presented the magnetic-field effects around the EI phase, where $\eta=1\,(\Leftrightarrow t_a=t_b)$. The magnetic field effects for smaller η are left for future work, where the magnetized SSO phase may be found because the LS/HS phase was obtained under a magnetic field with a mean-field analysis.[11)]

3.4 Entanglement entropy

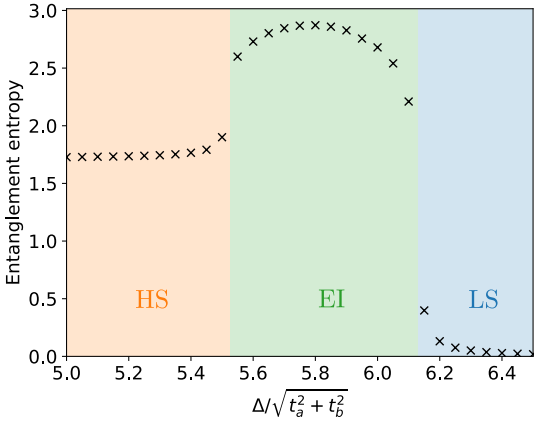

Fig. 7. Entanglement entropy in the HS, EI, and LS phases, where the system whose size is $L=60$ is devided into the left and right one whose size is $l=30$. The model parameters are $\eta=1.0\,(\Leftrightarrow t_a=t_b)$, $U/\sqrt{t_a^2+t_b^2}=12$, $U'=U-2J$ and $J=I$.

In this subsection, we present the properties of entanglement entropy in the HS, EI, and LS phases. Generally, entanglement entropy is sensitive to phase transitions, and is useful to determine the phase boundaries[28–30)]

Figure 7 shows the entanglement entropy as a function of crystal-field splitting. The entanglement entropy is defined for the density matrix of a 30 site subsystem in a 60 site system. The system has the periodic boundary condition. The truncation number in DMRG is set to $\chi=256$ for Fig. 7. We set $\eta=1.0\,(\Leftrightarrow t_a=t_b)$, $U/\sqrt{t_a^2+t_b^2}=12$, $U'=U-2J$ and $J=I$, which are the same as the parameters in the dashed line in Fig. 1(a).

The entanglement entropy in the HS phase is not far from $2\log 2\sim 1.39$. The picture of valence bond solid in the AKLT model[31)] can be applied to the picture in the HS phase. In this picture, the value of $2\log 2$ originates in the two valence bonds in the edges of the subsystem. In the EI phase, the entropy is larger than that in the HS and LS phases. The discontinuities of the entanglement entropy are found in the HS-EI and EI-LS phase boundaries. Based on these discontinuities, we determined the phase boundaries in Fig. 1 and Fig. 2. In the LS phase, the entropy is quite small. This is because the electrons in the LS phase cannot move due to the Pauli exclusion principle.

4. Summary

We made a ground-state phase diagram of the low-energy effective model of the one-dimensional two-orbital Hubbard model for the spin-crossover region on the basis of the density matrix renormalization group method. We found an excitonic insulating (EI) phase and spin-state ordering (SSO) phase in the intermediate region between a low-spin (LS) phase and a high-spin (HS) phase. The EI phase is realized in the region where $t_a/t_b \sim 1$, where t_a/t_b is the ratio of electron transfers, and the SSO phase is realized in the region where $t_a/t_b \ll 1$.

The spin correlation function in the EI phase has a peak wavenumber at $k = \pi \langle P_H \rangle$, resulting in a incommensurate spin correlation. The spin-state structure in the SSO phase shows the LS/HS/HS structure and various types of incommensurate structures depending on the crystal-field splitting.

We also made a phase diagram in a magnetic field. We found a spin gap not only in the LS and HS phases but also in the EI phase. The spin gap found in the EI phase is similar to the Haldane gap observed in the $s = 1$ Heisenberg model. We also found that the magnetization process in the EI phase has two stages, where the magnetization curve has different gradients corresponding to the phase transition, where the directions of $s = 1$ spins are fixed by a magnetic field.

Finally, we found the discontinuities of the entanglement entropy in the HS-EI and EI-LS phase boundaries, and these are useful to determine the boundaries.

Acknowledgements

We are grateful to M. Naka, J. Nasu, A. Ono, and Y. Masaki for their fruitful discussion and critical readings of the manuscripts. H. M. also acknowledges financial supports from KAKENHI No. 21K03380, CSRN and CSIS in Tohoku University.

1) M. Imada, A. Fujimori, and Y. Tokura: Rev. Mod. Phys. **70** (1998) 1039.
2) S. Yamaguchi, Y. Okimoto, H. Taniguchi, and Y. Tokura: Phys. Rev. B **53** (1996) R2926.
3) K. Asai, A. Yoneda, O. Yokokura, J. Tranquada, G. Shirane, and K. Kohn: J. Phys. Soc. Jpn. **67** (1998) 290.
4) R. Mahendiran and A. K. Raychaudhuri: Phys. Rev. B **54** (1996) 16044.
5) K. Sato, A. Matsuo, K. Kindo, Y. Kobayashi, and K. Asai: J. Phys. Soc. Jpn. **78** (2009) 093702.
6) J. Yu, D. Louca, D. Phelan, K. Tomiyasu, K. Horigane, and K. Yamada: Phys. Rev. B **80** (2009) 052402.
7) K. Oka, M. Azuma, W.-t. Chen, H. Yusa, A. A. Belik, E. Takayama-Muromachi, M. Mizumaki, N. Ishimatsu, N. Hiraoka, M. Tsujimoto, M. G. Tucker, J. P. Attfield, and Y. Shimakawa: J. Am. Chem. Soc. **132** (2010) 9438.
8) J. Kuneš and P. Augustinský: Phys. Rev. B **89** (2014) 115134.
9) J. Kuneš and P. Augustinský: Phys. Rev. B **90** (2014) 235112.
10) J. Nasu, T. Watanabe, M. Naka, and S. Ishihara: Phys. Rev. B **93** (2016) 205136.
11) T. Tatsuno, E. Mizoguchi, J. Nasu, M. Naka, and S. Ishihara: J. Phys. Soc. Jpn. **85** (2016) 083706.
12) D. Geffroy, A. Hariki, and J. Kuneš: Phys. Rev. B **97** (2018) 155114.
13) Y. Wakisaka, T. Sudayama, K. Takubo, T. Mizokawa, M. Arita, H. Namatame, M. Taniguchi, N. Katayama, M. Nohara, and H. Takagi: Phys. Rev. Lett. **103** (2009) 026402.
14) K. Seki, Y. Wakisaka, T. Kaneko, T. Toriyama, T. Konishi, T. Sudayama, N. L. Saini, M. Arita, H. Namatame, M. Taniguchi, N. Katayama, M. Nohara, H. Takagi, T. Mizokawa, and Y. Ohta: Phys. Rev. B **90** (2014) 155116.
15) T. Saitoh, Y. Yamashita, N. Todoroki, T. Kyômen, M. Itoh, M. Higashiguchi, M. Nakatake, and K. Shimada: J. Electron Spectrosc. Relat. Phenom. **144-147** (2005) 893.
16) M. M. Altarawneh, G.-W. Chern, N. Harrison, C. D. Batista, A. Uchida, M. Jaime, D. G. Rickel, S. A. Crooker, C. H. Mielke, J. B. Betts, J. F. Mitchell, and M. J. R. Hoch: Phys. Rev. Lett. **109** (2012) 037201.
17) A. Ikeda, T. Nomura, Y. H. Matsuda, A. Matsuo, K. Kindo, and K. Sato: Phys. Rev. B **93** (2016) 220401.
18) A. Ikeda, Y. H. Matsuda, and K. Sato: Phys. Rev. Lett. **125** (2020) 177202.
19) A. Sotnikov and J. Kuneš: Sci. Rep. **6** (2016) 30510.
20) J. Fujioka, Y. Yamasaki, H. Nakao, R. Kumai, Y. Murakami, M. Nakamura, M. Kawasaki, and Y. Tokura: Phys. Rev. Lett. **111** (2013) 027206.
21) J. Fujioka, Y. Yamasaki, A. Doi, H. Nakao, R. Kumai, Y. Murakami, M. Nakamura, M. Kawasaki, T. Arima, and Y. Tokura: Phys. Rev. B **92** (2015) 195115.
22) Y. Yamasaki, J. Fujioka, H. Nakao, J. Okamoto, T. Sudayama, Y. Murakami, M. Nakamura, M. Kawasaki, T. Arima, and Y. Tokura: J. Phys. Soc. Jpn. **85** (2016) 023704.
23) J. Kuneš: J. Phys.: Condens. Matter **27** (2015) 333201.
24) S. R. White: Phys. Rev. Lett. **69** (1992) 2863.
25) S. R. White: Phys. Rev. B **48** (1993) 10345.
26) Y. Kanamori, H. Matsueda, and S. Ishihara: Phys. Rev. Lett. **107** (2011) 167403.
27) T. Kaneko and Y. Ohta: Phys. Rev. B **90** (2014) 245144.
28) S. Ejima, T. Kaneko, Y. Ohta, and H. Fehske: Phys. Rev. Lett. **112** (2014) 026401.
29) F. Iemini, T. O. Maciel, and R. O. Vianna: Phys. Rev. B **92** (2015) 075423.
30) Y.-C. Li and Z.-G. Yuan: Phys. Lett. A **380** (2016) 272.
31) I. Affleck, T. Kennedy, E. H. Lieb, and H. Tasaki: Phys. Rev. Lett. **59** (1987) 799.